

# Divergent growth of poly(amidoamine) dendrimer- like branched polymers at the reducing end of cellulose nanocrystals

Maud Chemin, Céline Moreau, Bernard Cathala, Ana Villares\*

UR1268 BIA, INRAE, F-44316, Nantes, France

## ABSTRACT

This paper presents the growth of dendritic polymers at the reducing ends of cellulose nanocrystals by the “grafting from” approach. We took advantage of the chemically differentiated ends of cellulose nanocrystals to specifically synthesize dendrimers at their reducing end by the divergent approach. We used acid-amine coupling reactions in aqueous media to synthesize the carboxylic acid- or amine-terminated poly(amidoamine) dendrimers. The growth of dendrimer generations was monitored by UV and FTIR spectroscopies, and we successfully introduced up to 4 generations. The dendrimer growth at reducing ends was demonstrated by the nanocrystal adsorption driven by the peripheral amino groups onto gold surfaces. Hence, the results from quartz crystal microbalance with dissipation (QCM-D) pointed to a rather upright orientation of the dendrimer-modified cellulose nanocrystals. As the generation increased, the adsorbed layers appeared to be more flexible, which demonstrated that the functionality at the reducing end can successfully tune the properties of cellulose nanocrystals.

**Keywords:** tunicate cellulose nanocrystals; reducing end functionalization; poly(amidoamine) dendrimer; oriented adsorption.

22

## 23 **1. Introduction**

24 Cellulose nanocrystals (CNC) have gained prominence as bio-based materials for a wide range  
25 of applications (Charreau, H., Cavallo, E., & Foresti, M. L., 2020) thanks to their mechanical and  
26 barrier properties, liquid crystal behavior, optical properties, and amphiphilic characteristics  
27 (Eichhorn, S. J., 2011; Heise, K. et al., 2020; Lin, N., Huang, J., Chang, P. R., Anderson, D. P.,  
28 & Yu, J., 2011). CNC are obtained from cellulose fibers by acid hydrolysis that preferentially  
29 solubilizes the disordered regions of cellulose, resulting in rod-like crystallites with cross-  
30 sections in the nanoscale (5-20 nm) and aspect ratio values in the 5-50 range (Sacui, I. A. et al.,  
31 2014). One of the particularities of cellulose is the orientation of the chains within the crystal  
32 structure yielding two chemically differentiated ends. Indeed, the parallel arrangement of  
33 cellulose chains in the cellulose I allomorph results in C1 reducing ends (aldehyde  
34 functionalities) at one end of the nanocrystal, and C4 hydroxyl groups at the opposite end.  
35 Taking advantage of this chemical polarity (hydroxyl versus aldehyde), the selective  
36 modification of CNC reducing ends has recently attracted much attention (Heise, Katja et al.,  
37 2020; Tao, H., Lavoine, N., Jiang, F., Tang, J., & Lin, N., 2020) However, there are still very  
38 few studies focusing on the growth of functionalities at reducing ends by the “grafting from”  
39 approach (Delepierre, G. et al., 2021; Risteen, B. et al., 2018; Zoppe, J. O. et al., 2017).  
40 Generally, the polymerization initiator is introduced at the reducing end and the subsequent  
41 addition of the monomers yields to the polymeric functionality. This article describes for the first  
42 time the synthesis of poly(amidoamine) dendrimers at the CNC reducing ends by the “grafting  
43 from” approach. Our strategy involves straightforward acid-amine coupling reactions, and CNC  
44 act as solid support to immobilize the core and grow dendrimer generations.

45 Dendrimers are regular hyperbranched polymers synthesized from a multi-functional core by  
46 repeated cycles of synthesis. They are characterized by the number of branches (generation) and  
47 the peripheral functional groups (amino, carboxyl, hydroxyl or hydrocarbon groups). Therefore,  
48 dendrimers display multiple peripheral functional groups giving rise to multivalencies and a  
49 tunable size depending on dendritic generation. Hence, dendrimers have found many  
50 applications in different fields as nanoscaffolds for targeted drug delivery, and templates for the  
51 fabrication of metal nanoparticles (Guo, Y. Q., Shen, M. W., & Shi, X. Y.; Nikzamid, M.,  
52 Hanifehpour, Y., Akbarzadeh, A., & Panahi, Y.). The grafting of dendrimers on cellulose offers  
53 many advantages resulting from its promising properties such as biodegradability,  
54 biocompatibility, and availability. Poly(propylene imine) (PPI) and poly(amidoamine)  
55 (PAMAM) dendrimers have been grown on the CNC surface by iterative Michael additions  
56 (Golshan, M., Salami-Kalajahi, M., Roghani-Mamaqani, H., & Mohammadi, M., 2017; Hassan,  
57 M. L., 2006; Tehrani, A. D. & Basiryani, A., 2015; Wang, Y. C. & Lu, Q. Y., 2020). In those  
58 studies, dendrimers covered the whole CNC surface and changed significantly their surface  
59 properties, inducing CNC aggregation. In this work, we specifically synthesized dendrimers at  
60 the CNC reducing end, thus retaining the CNC surface properties while adding the dendritic  
61 functionalities at one end. As previously showed, the introduction of functionalities at the CNC  
62 reducing ends allows the supramolecular assembly by this end, and tunes the responsiveness  
63 (Chemin, M., Moreau, C., Cathala, B., & Villares, A., 2020; Chemin, Maud, Moreau, Céline,  
64 Cathala, Bernard, & Villares, Ana, 2020; Lokanathan, A. R. et al., 2013; Villares, A., Moreau,  
65 C., & Cathala, B., 2018). This work opens new perspectives for CNC applications, by their  
66 patchy modification to achieve the desired functionality at the reducing end.

67

68

69

70

## 71 **2. Materials and methods**

### 72 *2.1. Cellulose nanocrystals preparation*

73 Cellulose nanocrystals (t-CNC) were obtained from tunicates (*Styela clava*) collected on the  
74 coast of Quimiac (France) and prepared and characterized as previously described (Chemin, M.  
75 et al., 2020; Chemin, Maud et al., 2020; Villares, A. et al., 2018). The surface charge density,  
76 calculated by conductometric titration (TIM900 titration manager and CDM230 conductimeter),  
77 was  $0.022 \pm 0.001 \text{ mmol g}^{-1}$ .

### 78 *2.2. Materials*

79 *N*-(3-dimethylaminopropyl)-*N*-ethylcarbodiimide hydrochloride (EDC), *N*-hydroxysuccinimide  
80 (NHS), hexamethylenediamine (HMDA) (98%), trimesic acid (TMA) (95%), sodium chlorite  
81 ( $\text{NaClO}_2$ ), acetic acid, potassium chloride (KCl) and potassium hydroxide (KOH) were  
82 purchased from Sigma-Aldrich (France) and were used without further purification. Dialysis  
83 membrane, molar mass cut off 12-14 kDa, was purchased from Spectrum Laboratories Inc.  
84 Water was purified by Millipore Milli-Q purification system (18.2 M $\Omega$ ).

### 85 *2.3. Methods*

#### 86 *2.3.1. Introduction of amine moieties.*

87 Prior to the first step of functionalization, the aldehyde groups on the reducing end of t-CNCs  
88 were oxidized to carboxylic acid groups as previously described (Chemin, M. et al., 2020;  
89 Chemin, Maud et al., 2020; Villares, A. et al., 2018). Briefly, t-CNC (200 mL at  $6.9 \text{ g L}^{-1}$ ) were  
90 oxidized by the addition of 33.7 mmol of  $\text{NaClO}_2$ , and the pH was adjusted to 3.5 using 1 M

91 acetic acid, followed by stirring for 20 h at room temperature. The reaction mixture was purified  
92 by centrifugation (20000 g, 20 °C, 60 min) followed by dialysis (molar mass cut off 12-14 kDa)  
93 against milli-Q water for 10 days. Dispersions were stirred in water for 24 h to avoid nanocrystal  
94 aggregation.

95 Afterwards, amine moieties were introduced using the NHS/EDC amide coupling with  
96 hexamethylenediamine (Lokanathan, A. R., Lundahl, M., Rojas, O. J., & Laine, J., 2014). A 2 g  
97 L<sup>-1</sup> suspension of oxidized t-CNC was degassed by bubbling nitrogen for 20 min, and NHS (50  
98 mmol) was added, followed by EDC (5 mmol), and the pH was checked to be close to 6.5.  
99 Appropriate amounts of KCl were added such that the final suspension was 0.5 M.  
100 Hexamethylenediamine was added in large excess (5 mmol) to avoid the grafting of two t-CNCs  
101 on the same molecule. Then, pH was checked to be above 9.2. The reaction was incubated under  
102 magnetic stirring at room temperature for 24 h. Amine-functionalized t-CNCs were purified by  
103 centrifugation (20000 g, 60 min, 20 °C) and then dialyzed (molar mass cut off 12-14 kDa)  
104 against Milli-Q water for 5 days. After dialysis, dispersions were stirred in water for 24 h to  
105 avoid nanocrystal aggregation.

### 106 2.3.2. *Introduction of acid moieties*

107 A similar procedure was applied to graft trimesic acid on the amine-functionalized t-CNCs.  
108 Appropriate amounts of KCl were added to the suspension of amine-functionalized t-CNCs such  
109 that the final suspension was 0.5 M and the dispersion was stirred under nitrogen bubbling for 20  
110 min. A 0.95 g L<sup>-1</sup> solution of trimesic acid in water was degassed by bubbling nitrogen for 5 min,  
111 NHS were added (3 mmol), followed by EDC (15 mmol) under stirring and bubbling nitrogen.  
112 Both suspensions were then mixed with a final t-CNC concentration of 1.5 g L<sup>-1</sup> (5 mmol of  
113 amine groups). pH was checked to be above 9.2, and the reaction was incubated under magnetic

114 stirring at room temperature for 24 h. Acid-functionalized t-CNCs were purified by  
115 centrifugation (20000 g, 60 min, 20 °C) and then dialyzed (molar mass cut off 12-14 kDa)  
116 against Milli-Q water for 5 days. Dispersions were stirred in water for 24 h to avoid nanocrystal  
117 aggregation. After grafting, hybrid nanoparticles are denoted t-CNC-G $x$ ,  $x$  being the generation.  
118 When  $x$  is a decimal number, the peripheral groups are the carboxylic acid, and when  $x$  is an  
119 integer, the t-CNC peripheral groups are the amine functionalities. The step-by-step synthesis  
120 was repeated consecutively up to the synthesis of the fourth generation t-CNC-G4.

## 121 2.4. Characterization

### 122 2.4.1. Scanning Transmission Electron Microscopy (STEM)

123 t-CNC dispersions were diluted to 0.2 g L<sup>-1</sup> in KOH 1 mM and deposited on freshly glow-  
124 discharged carbon-coated electron microscope grids (200 mesh, Delta Microscopies, France).  
125 Water excess was removed by blotting (Whatman filter paper). The grids were dried overnight in  
126 air at ambient temperature and then coated with platinum layer by an ion-sputter coater  
127 (thickness = 0.5 nm). The grids were observed with a Quattro Scanning electron microscopy  
128 (Thermo Scientific) with a STEM detector, working at 10kV.

129 2.4.2. *Elemental analysis.* t-CNCs were freeze-dried and the resulting powder (10 mg) was  
130 placed in tin capsules for analysis. The total C, N, and S contents of t-CNCs were determined by  
131 a C/N/S analyzer (Vario Micro cube, Elementar) coupled to a gas chromatographic system and a  
132 thermal conductivity detector (TCD). Nitrogen content was determined by the Dumas' method  
133 combustion (Shea, F. & Watts, C. E., 1939).

### 134 2.4.3. Infrared spectroscopy

135 Infrared spectra were obtained from KBr pellets containing freeze-dried t-CNC and t-CNC-G $x$   
136 samples placed directly in a Nicolet iS50 FTIR spectrometer (Thermo Scientific) in absorbance

137 mode. All spectra were recorded using OMNIC software with a  $4\text{ cm}^{-1}$  resolution after 200  
138 continuous scans from 400 to  $4000\text{ cm}^{-1}$ . All samples were acidified with HCl 100 mM in order  
139 to protonate carboxylic acids.

#### 140 2.4.4. *UV-visible spectroscopy*

141 UV-visible spectra were obtained from t-CNC-Gx suspensions at  $0.3\text{ g L}^{-1}$  in KOH 1mM using a  
142 quartz cell placed directly in a SPECORD S 600 spectrometer (Analytik Jena GmbH). All  
143 spectra were recorded using WinASPECT software set to absorbance mode after 10  
144 accumulations and scanning from 200 to 1000 nm. A reference sample consisting of t-CNC at  
145  $0.3\text{ g L}^{-1}$  in KOH 1mM mixed with trimesic acid at  $0.001\text{ g L}^{-1}$  in KOH 1 mM was used for  
146 comparison.

#### 147 2.4.5. *Thermal degradation*

148 Thermogravimetric analysis (TGA) were performed under a nitrogen atmosphere using a TA  
149 instruments TGA2050. Samples (5 mg) were equilibrated at  $60^{\circ}\text{C}$  for 10 minutes and heated  
150 from 60 to  $600^{\circ}\text{C}$  at a heating rate of  $5^{\circ}\text{C min}^{-1}$ .

#### 151 2.4.6. *Surface Plasmon Resonance (SPR)*

152 The SPR measurements were performed with a Biacore x100 (GE Healthcare, Sweden) with a  
153 continuous flow system. The SPR technique is based on the phenomenon of total internal  
154 reflection of light. The adsorption of dendrimer-modified t-CNC onto the sensor surface  
155 produces a shift in the optical resonance properties of the sensor, which results in an increase of  
156 the SPR angle where the reflected light intensity is in its minimum (Schoch, R. L. & Lim, R. Y.  
157 H., 2013). All measurements were carried out using gold sensors at  $20^{\circ}\text{C}$  with a  $0.3\text{ g L}^{-1}$   
158 dispersion of t-CNC in KOH 1mM at  $10\text{ }\mu\text{L min}^{-1}$ . The amount of adsorbed dendrimer-modified

159 t-CNC,  $\Gamma$ , was then calculated from the SPR angle shift,  $\Delta\theta$ , according to the following  
160 expression (Kontturi, K. S., Kontturi, E., & Laine, J., 2013):

$$161 \quad \Gamma = \frac{l_d}{2} \frac{\Delta\theta}{m(dn/dc)} \quad (1)$$

162 Where  $l_d$  is the characteristic evanescent electromagnetic field decay length (281.2 nm),  $m$  is the  
163 sensitivity factor for the sensor (102.5° per RIU) obtained after calibration, and  $dn/dc$  is the  
164 refractive index increment (0.15 mL g<sup>-1</sup>). Results are expressed as the mean of two experiments.

#### 165 2.4.7. Quartz crystal microbalance with dissipation monitoring (QCM-D)

166 QCM-D measurements were performed with a Q-Sense E4 instrument (AB, Sweden) using a  
167 piezoelectric AT-cut quartz crystal coated with gold electrodes on each side (QSX301, Q-Sense),  
168 as previously described (Chemin, Maud et al., 2020; Villares, A. et al., 2018). All measurements  
169 were carried out using the QCM flow cell modules at 20 °C with a 0.3 g L<sup>-1</sup> dispersions of t-  
170 CNC in KOH 1 mM at 100 μL min<sup>-1</sup>. Frequency ( $\Delta f_n/n$ ) and ( $\Delta D_n$ ) dissipation changes were  
171 simultaneously registered at 5 MHz fundamental resonance frequency and its several overtones  
172 as a function of time. Any material adsorbed on the crystal surface induces a decrease of the  
173 resonance frequency. If the adsorbed mass is evenly distributed, rigidly attached and small  
174 compared to the mass of the crystal,  $\Delta f$  is directly proportional to the adsorbed mass ( $\Delta\Gamma$ ) using  
175 the Sauerbrey's equation (Sauerbrey, G., 1959):

$$176 \quad \Delta\Gamma = -C \frac{\Delta f}{n} \quad (2)$$

177 where  $C$  is the constant for the mass sensitivity of the quartz crystal (0.177 mg m<sup>-2</sup> Hz<sup>-1</sup> at  $f_0 = 5$   
178 MHz) and  $n$  is the overtone number.



179 Dissipation signals were recorded simultaneously to frequency shifts and they provide a measure  
180 of the frictional losses due to the viscoelastic properties of the adsorbed layer. The overtone  $n = 5$   
181 was used for comparing the adsorption of unmodified and modified t-CNCs.

182

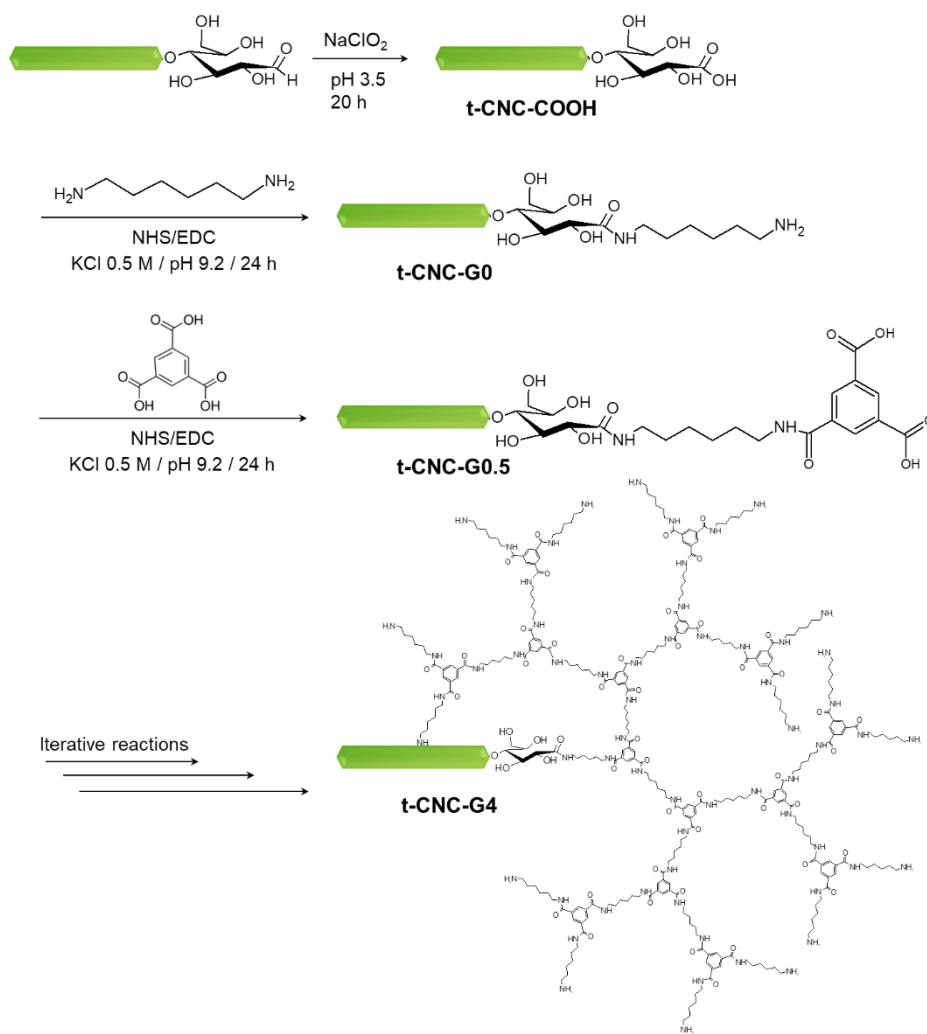
### 183 **3. Results**

#### 184 *3.1. Dendritic synthesis at t-CNC reducing end*

185 Cellulose nanocrystals can be viewed as rigid rod-like crystals with two chemically differentiated  
186 ends. Hence, reducing ends display aldehyde groups whereas the non-reducing ends present the  
187 less reactive hydroxyl groups. This chemical asymmetry allows the selective introduction of  
188 functionalities at the reducing end of cellulose nanocrystals (Lin, F., Cousin, F., Putaux, J.-L., &  
189 Jean, B., 2019; Lokanathan, A. R. et al., 2013; Villares, A. et al., 2018). In this work, we have  
190 used tunicate cellulose nanocrystals (t-CNC) as a solid support for the divergent synthesis of  
191 poly(amidoamine) dendrimers at the t-CNC reducing ends. Tunicate cellulose nanocrystals were  
192 selected because they are quasi-perfect monocrystals and, besides their narrow distribution in  
193 cross-section and length dimensions, they have a rectangular  $8.8 \text{ nm} \times 18.2 \text{ nm}$  cross-sectional  
194 shape (Terech, P., Chazeau, L., & Cavaille, J. Y., 1999). As the monomers, we selected a  
195 diamine, the hexamethylenediamine (HMDA), and a tricarboxylic acid, the trimesic acid (TMA).  
196 Therefore, dendrimer growth was driven by TMA, whereas the HMDA grafting only changed  
197 the peripheral functional groups.

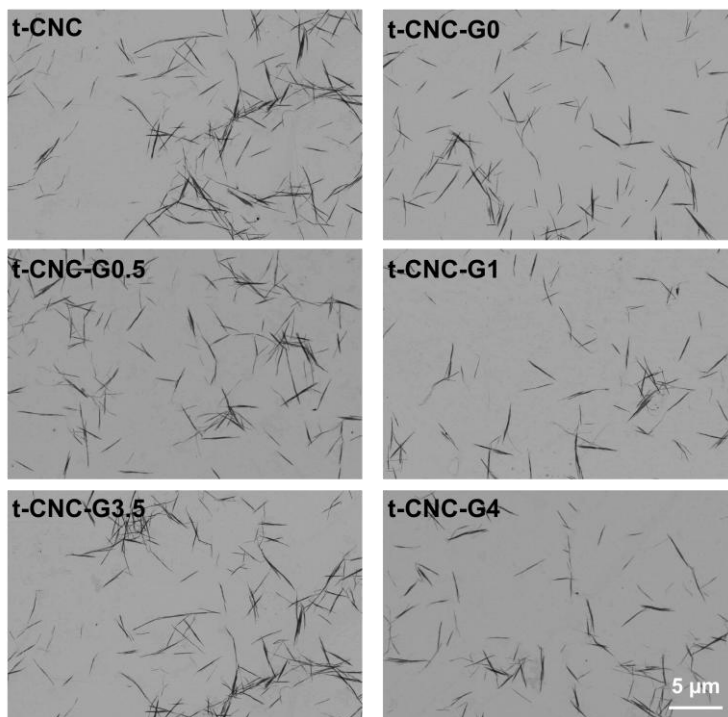
198 Our synthetic approach first involved the oxidation of t-CNC aldehyde groups into carboxylic  
199 acids and the subsequent dendrimer growth by the *N*-(3-dimethylaminopropyl)-*N*-  
200 ethylcarbodiimide hydrochloride (EDC) chemistry. Fig. 1 shows the theoretical dendrimer  
201 generation growth at the reducing end of cellulose nanocrystals. EDC-activated carboxylic acids

202 were transformed into amine functionalities by their reaction with hexamethylenediamine.  
203 HMDA was added in high excess to avoid cross-linking. Furthermore, reactions were carried out  
204 above pH 9.2 and at high ionic strength (KCl 0.5 M) to screen t-CNC interactions and avoid  
205 unspecific adsorption of chemicals. The second step was the reaction of amine-functionalized t-  
206 CNC with trimesic acid. Reaction was carried out under similar conditions, TMA was EDC-  
207 activated and added to amino-t-CNC dispersed in high ionic strength solutions (KCl 0.5 M) at  
208 pH 9.2. This two-step procedure was repeated 4 times to achieve the amine-terminated  
209 generation 4 (t-CNC- G4).



211 **Fig. 1.** Scheme of the divergent dendrimer synthesis on the reducing ends of t-CNC by the  
212 successive grafting of HMDA and TMA by EDC/NHS activation. In the scheme, t-CNC are  
213 represented as green rods. Dimensions of t-CNC, HMDA and TMA are not scaled.

214  
215 Generally, poly(amidoamine) dendrimers are prepared by serial repetitions of the Michael  
216 addition of amine-functionalized CNCs (Golshan, M. et al., 2017; Hassan, M. L., 2006; Tehrani,  
217 A. D. & Basiryani, A., 2015). Recently, Wang et al. have described a protocol including a  
218 Michael addition followed by amination in methanol (Wang, Y. C. & Lu, Q. Y., 2020).  
219 However, in all cases, reactions were performed in methanol/water mixtures. Our approach  
220 involved successive amidation reactions with EDC/NHS activation and did not require the use of  
221 organic solvents or high temperatures. Reactions were entirely performed in aqueous media at  
222 room temperature. Purification and removal of soluble chemicals after each generation growth  
223 was facilitated by t-CNC precipitation. The high ionic strength (0.5 M) favored nanocrystal  
224 precipitation and then, salt was removed by dialysis. The recovered t-CNC masses after each  
225 reaction were higher than 99% for both the first oxidation and the successive EDC/NHS  
226 coupling. t-CNC-G<sub>x</sub> were stirred overnight in KOH 1 mM to avoid nanocrystal aggregation  
227 arising from the interaction between positively charged amino groups and the negative sulfate  
228 groups in the surface of t-CNC. As Fig. 2 shows, the morphology of t-CNC was not altered by  
229 the dendritic growth at their reducing ends, the t-CNC exhibited the typical and expected rod-like  
230 shape. The STEM images did not show significant differences between when the dendrimer was  
231 amino- or acid-terminated, and no significant association between nanocrystals was observed due  
232 to dendrimer growth. Hence, t-CNC can be viewed as a solid support to hold the dendrimer so  
233 the excess of chemicals can be easily removed by centrifugation and dialysis.



234  
 235 Fig. 2. STEM images of native t-CNC, amine-terminated (t-CNC-G0), the first acid- and amine-  
 236 terminated (G0.5 and G1, respectively) and last acid- and amine-terminated (G3.5 and G4,  
 237 respectively) dendrimer generations grown on t-CNC reducing ends.

238  
 239 The elemental compositions of t-CNC-G4 compared to native t-CNC (Table 1) revealed a  
 240 significant higher nitrogen content for t-CNC-G4. According to the carbon-nitrogen (C/N) ratio,  
 241 for t-CNC-G4 there was a nitrogen atom for each 45 glucose units. As the dendrimer G4 contains  
 242 62 nitrogen atoms, there was one dendrimer per 2800 glucose units. The degree of  
 243 polymerization (DP) of cotton cellulose nanocrystals is between 150 and 325 (Potthast, A. et al.,  
 244 2015); therefore, considering an elemental fibril formed by 16 cellulose chains and a high DP for  
 245 tunicate nanocrystals, there was approximately 1.6 dendrimers for each cellulose nanocrystal.  
 246 This high degree of substitution could be explained by the introduction of several dendrimer

247 functionalities at the reducing end, or by some degree of chain breakdown during reactions that  
248 created new reducing ends.

249

250 Table 1

251 Elemental compositions and elemental C/N ratios for native t-CNC and t-CNC-G4.

252 Determinations were made in triplicate and results are expressed as the mean  $\pm$  standard  
253 deviation.

	N (%)	C (%)	S (%)	C/N
t-CNC	$0.002 \pm 0.002$	$43.925 \pm 0.686$	$0.485 \pm 0.169$	$9050 \pm 764$
t-CNC-G4	$0.186 \pm 0.002$	$43.090 \pm 0.127$	$0.305 \pm 0.064$	$232 \pm 1$

254

255 Fig. 3 shows the FTIR spectra of native t-CNC and t-CNC-G<sub>x</sub> for the first generations (G0.5 and

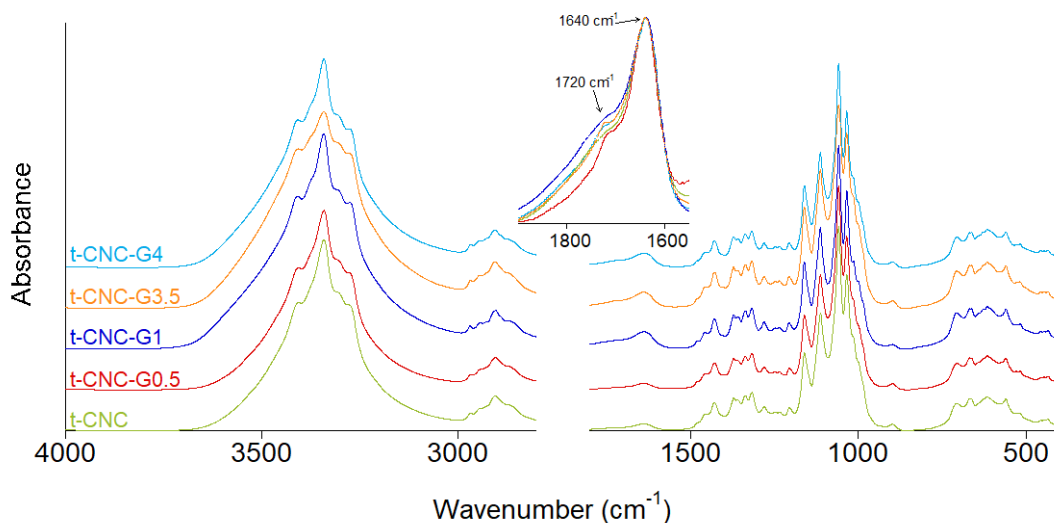
256 G1) and the last ones (G3.5 and G4). The FTIR spectrum of native t-CNCs (green bottom trace)

257 showed the characteristic bands of cellulose nanocrystals (Zhao, Y. & Li, J., 2014; Zhao, Y. D.,

258 Zhang, Y. J., Lindstrom, M. E., & Li, J. B., 2015). Upon dendrimer growth, the FTIR profile was

259 not modified, which indicated that the crystalline order of t-CNC was not altered by reducing end

260 modification.

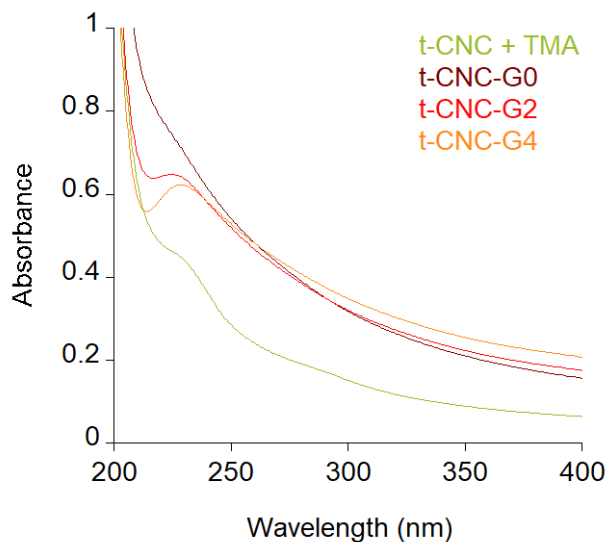


261  
 262 **Fig. 3.** FTIR spectra in absorbance of native t-CNC and the first acid- and amine-terminated  
 263 (G0.5 and G1, respectively) and last acid- and amine-terminated (G3.5 and G4, respectively)  
 264 dendrimer generations grown on t-CNC reducing ends.

265  
 266 The dendrimer growth was suggested by the increase in the C=O stretching band. For acid-  
 267 terminated generations (G0.5 and G3.5), FTIR spectra showed a new peak at  $1720\text{ cm}^{-1}$ , which  
 268 corresponded to the C=O stretching band of COOH groups. The intensity of this band increased  
 269 with generation, which pointed at dendritic growth. In the case of amine-terminated generations  
 270 (G1 and G4), the peak from COOH had decreased in intensity compared to their precursors,  
 271 indicating their partial transformation into amide forms. The spectra showed an increase in the  
 272 shoulder intensity at  $1700\text{ cm}^{-1}$ , which can be ascribed to the C=O stretching from amide I  
 273 bonding at  $1645\text{ cm}^{-1}$  (Benkaddour, A., Journoux-Lapp, C., Jradi, K., Robert, S., & Daneault, C.,  
 274 2014). However, this small signal from the amide bonds would be overlapped with the band at  
 275  $1635\text{ cm}^{-1}$  corresponding to the symmetric deformation vibration of adsorbed water molecules  
 276 (Schwanninger, M., Rodrigues, J. C., Pereira, H., & Hinterstoisser, B., 2004). On the other hand,

277 the bands of the C-N stretching and N-H deformation from amide II at  $1545\text{ cm}^{-1}$  were not  
278 detected.

279 Dendritic growth was also demonstrated by the increase in the UV absorption band at 228 nm  
280 corresponding to TMA. Fig. 4 shows the absorbance spectra of a mixture of native t-CNC and  
281 TMA, and t-CNC-G0, t-CNC-G2 and t-CNC-G4.



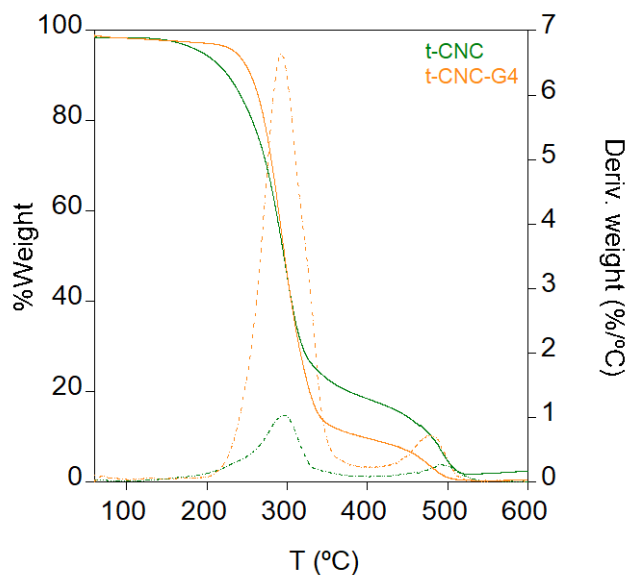
282  
283 **Fig. 4.** Absorbance spectra of free TMA in a native t-CNC dispersion, and the dendrimer  
284 generations t-CNC-G0, t-CNC-G2 and t-CNC-G4.

285  
286 The grafting of TMA on t-CNC resulted in an increasing baseline at low wavelengths possibly  
287 due to slight aggregation of nanocrystals, as well as the appearance of a shoulder at 280 nm  
288 ascribed to the TMA absorption band. When the generations increased, the shoulder at 280 nm  
289 become progressively more pronounced and, for the last generation, t-CNC-G4, a well-resolved  
290 band was observed. The possibility of unspecific adsorption of chemicals (HMDA and TMA) on  
291 the cellulose surface was discarded because in all cases, HMDA and TMA were added in high  
292 excess and t-CNC were thoroughly washed for their removal after reactions. Therefore, if

293 chemicals were adsorbed on t-CNC we would not see the step-by-step increase of FTIR and UV  
294 absorption bands.

295 t-CNC-G4 was further studied by thermogravimetric analysis to compare with native t-CNC  
296 (Fig. 5). The thermal analysis showed a two-step thermal degradation process, as previously  
297 described for cellulose nanocrystals (Lin, N. & Dufresne, A., 2014). First, the pyrolysis is  
298 catalyzed by the sulfate groups present on the t-CNC surface and then residues are carbonized  
299 (Wang, N., Ding, E. Y., & Cheng, R. S., 2007). The degradation profiles of native t-CNC and t-  
300 CNC-G4 were similar with a slight difference in the temperature that degradation started. For  
301 native t-CNC, thermal degradation started at 160 °C whereas for t-CNC-G4 degradation began at  
302 215 °C, while it ended at 360 °C for both, meaning that the degradation of t-CNC-G4 is faster  
303 (confirmed by a much more intense peak for the differential thermogravimetric (DTG) curve). In  
304 the DTG curve, represented by the weight derivative (%/°C), both native t-CNC and t-CNC-G4  
305 showed prominent pyrolysis process with two step degradation processes at 295 and 495 °C for  
306 native t-CNC and 293 and 480 °C for t-CNC-G4. The slight but significant differences in the  
307 thermal stability profile when the dendrimers were synthesized at the reducing ends of t-CNC  
308 could be due to the dendrimer functionalization.





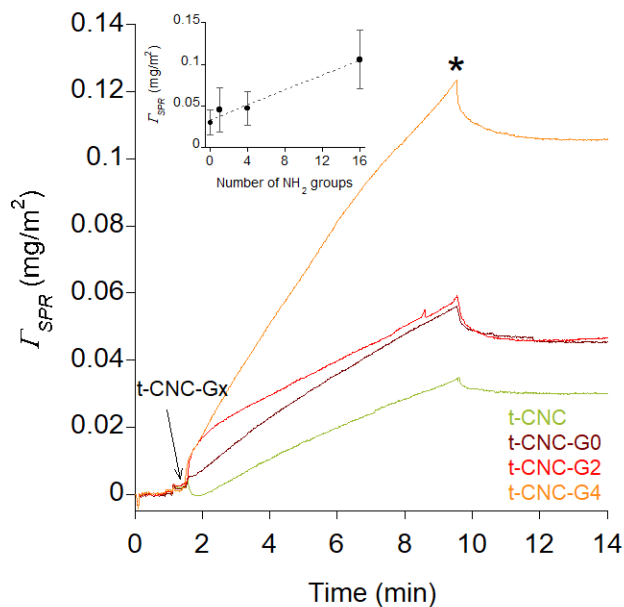
309

310 **Fig. 5.** Thermal gravimetric analysis (TGA) and first derivative of the TGA (differential  
 311 thermogravimetric, DTG) curves of native t-CNC and t-CNC-G4.

312

### 313 3.2. Reducing-end driven supramolecular assembly

314 The affinity of amine groups for gold was used to demonstrate the dendrimer growth at the  
 315 reducing ends of t-CNCs. Hence, the amine-terminated t-CNC-G0, t-CNC-G2 and t-CNC-G4  
 316 were adsorbed onto gold surfaces, and the adsorption process was monitored by surface plasmon  
 317 resonance (SPR). SPR is an optical technique based on the resonant oscillation of conduction  
 318 electrons at the interface between the gold surface and the t-CNC adsorbed layer when  
 319 stimulated by incident light. Hence, when the gold surface is modified by t-CNC adsorption, the  
 320 angle at which the plasmon is excited ( $\Delta\theta$ ) changes (Ahola, S., Myllytie, P., Osterberg, M.,  
 321 Teerinen, T., & Laine, J., 2008). The adsorbed mass can be calculated from the SPR angle shift,  
 322 according to Equation 1. Fig. 6 shows the adsorbed mass as a function of time for the adsorption  
 323 of native t-CNC and the amine-terminated dendrimers t-CNC-G0, t-CNC-G2 and t-CNC-G4  
 324 onto gold surfaces.



325  
 326 **Fig. 6.** Calculated surface coverage ( $\Gamma_{SPR}$ ) from SPR angle shift as a function of time showing  
 327 the adsorption of native t-CNC and the amine-terminated dendrimers t-CNC-G0, t-CNC-G2 and  
 328 t-CNC-G4. The arrow indicates the injection and the asterisk the rinsing step. The inset depicts  
 329 the relationship between surface coverage and the number of amine groups on the dendrimer.

330  
 331 The injection of native t-CNC resulted in a slight increase of the adsorbed mass, which indicated  
 332 some unspecific and very limited adsorption onto the gold surface. The first generation t-CNC-  
 333 G0 showed a similar profile to unmodified t-CNC but the surface coverage was higher. t-CNC-  
 334 G0 only contained one amine group at the reducing end; therefore, the SPR profile could be due  
 335 to a very slight adsorption on the gold surface. For t-CNC-G2, after injection, we observed a  
 336 deep increase in the angle shift and therefore the adsorbed mass, even if at the end of the  
 337 adsorption process, the surface coverage was similar to that of t-CNC-G0. Finally, the last  
 338 generation t-CNC-G4 showed the largest increase in mass after injection that continued  
 339 increasing towards a greater adsorbed mass. In all cases, the rinsing step resulted in a slight

340 decrease of the adsorbed mass, indicating low t-CNC-G<sub>x</sub> desorption and demonstrating the  
341 stability of the adsorbed nanoparticles. The SPR results clearly demonstrated the dendrimer  
342 generation growth. Table 2 shows the surface coverage at the end of the adsorption process. In  
343 previous studies, we had demonstrated that the adsorption of reducing end-modified t-CNC was  
344 impacted by the probability of the nanocrystal to have the proper orientation to adsorb (Chemin,  
345 M. et al., 2020). Hence, reducing end-modified t-CNC should be rather perpendicular to the  
346 surface, with the reducing end close enough to the surface to facilitate interactions and the  
347 subsequent adsorption. The dendrimer generation growth increased the number of amino groups  
348 at the t-CNC reducing ends, increasing the size and therefore boosting the probability to  
349 encounter the surface. This assumption was demonstrated by the linear relationship between the  
350 number of amino groups and the surface coverage calculated by SPR (inset of Fig. 6).

351 In order to get more insight into the arrangement of amine-terminated t-CNC-G<sub>x</sub> on the gold  
352 substrate, their adsorption was monitored by quartz crystal microbalance with dissipation (QCM-  
353 D). The evolution of frequency ( $\Delta f_n/n$ ) and dissipation ( $\Delta D_n$ ) signals for the overtone number  $n =$   
354 5 as a function of time for t-CNC-G0, t-CNC-G2 and t-CNC-G4 dispersions are shown in Fig. 7a  
355 and b. In all cases, the frequency decrease upon t-CNC-G<sub>x</sub> injection was very low (from -1 to -3  
356 Hz), indicating a very small t-CNC-G<sub>x</sub> mass adsorbed on the gold substrate (Moreau, C., Beury,  
357 N., Delorme, N., & Cathala, B., 2012). In previous studies, we have already shown that  
358 unmodified CNC did not adsorb on gold substrates (Chemin, Maud et al., 2020; Villares, A. et  
359 al., 2018), which showed that the adsorption was driven by the functionalities at the reducing  
360 ends. The frequency decrease reflected the t-CNC-G<sub>x</sub> adsorbed mass together with the hydrating  
361 water. Therefore, the surface coverage calculated from QCM-D by the Sauerbrey's expression  
362 (equation 2) was in all cases higher than those calculated from SPR data (Table 2).

363

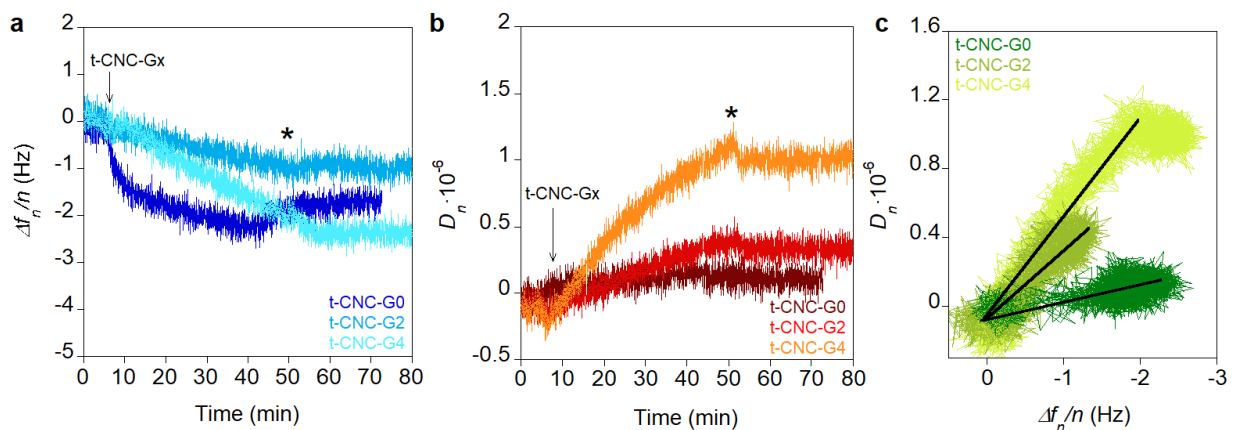
364 **Table 2**

365 Surface coverage calculated from SPR measurements ( $\Gamma_{SPR}$ ) and QCM-D frequency ( $\Gamma_{QCM}$ ) for  
366 the amine-terminated dendrimers t-CNC-G0, t-CNC-G2 and t-CNC-G4. Results are expressed as  
367 mean  $\pm$  standard deviation

	$\Gamma_{SPR}$ (mg m <sup>-2</sup> )	$\Gamma_{QCM}$ (mg m <sup>-2</sup> )
t-CNC-G0	0.046 $\pm$ 0.026	0.296 $\pm$ 0.056
t-CNC-G2	0.047 $\pm$ 0.020	0.099 $\pm$ 0.054
t-CNC-G4	0.106 $\pm$ 0.036	0.187 $\pm$ 0.159

368

369 QCM-D allows monitoring dissipation changes concomitantly with frequency variations. Hence,  
370 the different viscoelastic nature of the adsorbed t-CNC-Gx nanoparticles was investigated by the  
371 change of dissipation as a function of frequency ( $\Delta D_n$  vs  $\Delta f_n/n$ ). Fig. 7c shows the  $\Delta D_n$  vs  $\Delta f_n/n$   
372 plots for the adsorption of t-CNC-G0, -G2 and -G4. Usually, a small slope value of the  $\Delta D_n$  vs  
373  $\Delta f_n/n$  curve indicates a relatively thin and rigid adsorbed layer whereas high slope values are  
374 characteristic of thicker and viscoelastic layers (Kishani, S., Vilaplana, F., Ruda, M., Hansson,  
375 P., & Wagberg, L., 2020; Rodahl, M. et al., 1997).



376

377 **Fig. 7.** Frequency ( $\Delta f_n/n$ ) and dissipation ( $\Delta D_n$ ) changes for the overtone  $n = 5$  monitored by  
378 QCM-D during adsorption of t-CNC-G0, t-CNC-G2 and t-CNC-G4: (a) frequency as a function  
379 of time; (b) dissipation as a function of time; and (c)  $\Delta D_n$  vs  $\Delta f_n/n$  plots. The arrow indicates the  
380 injection of t-CNCs and the asterisk the rinsing step.

381  
382 The slopes values were 0.09, 0.33 and  $0.49 \cdot 10^{-6} \text{ Hz}^{-1}$  for t-CNC-G0, t-CNC-G2 and t-CNC-G4,  
383 respectively. The increase in the slope values as the generation grew indicated higher  
384 viscoelasticity of the anchoring group for higher dendrimer generations. This illustrated that the  
385 dendrimer size and the number of peripheral amino groups at the reducing ends of t-CNC  
386 determined the viscoelastic properties and therefore the interaction between t-CNC-Gx and the  
387 surface. Hence, as the generation increased, the t-CNC-Gx could have more freedom to form  
388 more flexible layers. It has been previously postulated that the reducing end-modified CNC  
389 adsorb on the gold surface by their functionality at the reducing end, and repel each other  
390 electrostatically due to the sulfate groups on the CNC surface, resulting in a rather upright  
391 orientation (Chemin, Maud et al., 2020; Lokanathan, A. R. et al., 2013; Villares, A. et al., 2018).  
392 In previous studies on the “grafting onto” of PAMAM dendrimers on CNC reducing ends, we  
393 have observed an increase in the  $\Delta D_n$  vs  $\Delta f_n/n$  slope as the dendrimer generation increased  
394 (Chemin, Maud et al., 2020). In this study, we obtained similar slope values, and the gradual  
395 increase observed for t-CNC-G0 to t-CNC-G4 could point at a different adsorption regimes as  
396 the generation increased. Indeed, the generation growth results in a higher number of amino  
397 groups together with an increase of the dendrimer volume and flexibility compared to the rigid  
398 nanocrystal. This was reflected by the increasing dissipation values, which was a supplementary  
399 proof to demonstrate the dendrimer growth at the reducing end.

400

#### 401 **4. Discussion**

402 The chemical polarity of cellulose nanocrystals has motivated the selective introduction of  
403 functionalities at only one end of the rod-like CNCs (Lin, F. et al., 2019; Lokanathan, A. R. et  
404 al., 2013; Villares, A. et al., 2018). The high reactivity of the aldehyde provides a specific  
405 anchoring point for chemical synthesis. Generally, macromolecules are introduced by “grafting  
406 onto” reactions, which involve coupling reactions between the terminal aldehyde and the  
407 targeted polymer (Chemin, Maud et al., 2020; Lin, F. et al., 2019; Sipahi-Saglam, E., Gelbrich,  
408 M., & Gruber, E., 2003; Tang, C. X. et al., 2018; Tao, H., Dufresne, A., & Lin, N., 2019;  
409 Tavakolian, M. et al., 2019). Differently, the “grafting from” approach includes the introduction  
410 of initiator molecules to carry out polymerization. Despite the advantages in terms of  
411 controllable polymerization and versatility of available monomers, the “grafting from” strategy  
412 has been scarcely used for polymer growth at the CNC reducing end. Zoppe et al. described for  
413 the first time the polymers synthesis at the reducing ends of CNC (Zoppe, J. O. et al., 2017). The  
414 introduction of initiators at reducing ends and the subsequent addition of the monomers *N*-  
415 isopropylacrylamide (NIPAM), [2-(methacryloyloxy)ethyl]-trimethylammonium chloride  
416 (METAC) and sodium 4-vinylbenzenesulfonate (4-SS) yielded nanorods with one end-tethered  
417 polymer chains by atom transfer radical polymerization (ATRP). By a similar approach, the  
418 same group described the polymerization of the thermoresponsive poly(*N*-isopropylacrylamide)  
419 (PNIPAM) at the reducing ends of CNC (Risteen, B. et al., 2018).

420 In this work, we describe for the first time the *in situ* growth of poly(amidoamine) dendrimers at  
421 the reducing end of cellulose nanocrystals. Our synthetic approach involved straightforward  
422 reactions in aqueous media and purification was easily achieved by phase separation. The growth

423 of dendrimer generations was easily controlled by UV and FTIR spectroscopies, and we  
424 successfully introduced 4 generations. The better resolution of the FTIR band at  $1720\text{ cm}^{-1}$  for  
425 the acid-terminated generations permitted to distinguish between the peripheral groups, amino or  
426 carboxylic acid, of each generation.

427 The divergent approach has been previously used for grafting dendrimers onto the whole CNC  
428 surface. Hence, poly(propylene imine) (PPI) and poly(amidoamine) (PAMAM) have been  
429 prepared up to the fourth generation. CNC were firstly aminated and dendrimer growth was  
430 performed by iterative Michael additions (Golshan, M. et al., 2017; Hassan, M. L., 2006;  
431 Tehrani, A. D. & Basiryani, A., 2015; Wang, Y. C. & Lu, Q. Y., 2020). The grafting density in  
432 terms of amino groups was  $20.1\text{ mmol g}^{-1}$  for the fourth PPI generation (Golshan, M. et al.,  
433 2017) and  $3.54\text{ mmol g}^{-1}$  for the fourth PAMAM generation (Wang, Y. C. & Lu, Q. Y., 2020),  
434 both at the CNC surface. In both cases, the coverage of the CNC surface by the dendrimer  
435 moieties was high, which resulted in CNC aggregation (Golshan, M. et al., 2017; Wang, Y. C. &  
436 Lu, Q. Y., 2020). The advantage of growing dendrimers specifically at the reducing end is the  
437 possibility of preserving the CNC surface properties but introducing new functionalities at only  
438 one end. Furthermore, this patchy functionalization allows the supramolecular assembly of CNC  
439 by their reducing end, even if the grafting density was significantly lower ( $0.14\text{ mmol g}^{-1}$ ),  
440 resulting in hairy layers (Lokanathan, A. R. et al., 2013). Hence, this work demonstrates that the  
441 reducing end dendrimer-grafting allowed the adsorption of t-CNC-G<sub>x</sub> onto gold surfaces by their  
442 modified reducing end. This is of special importance for designing novel materials by  
443 supramolecular assembly where CNC can be specifically bound by one end.

444

## 445 **5. Conclusions**

446 This work describes a straightforward “grafting onto” strategy to synthesize poly(amidoamine)  
447 dendrimers at the reducing ends of tunicate cellulose nanocrystals. The generation growth was  
448 monitored by UV and FTIR spectroscopies. This work demonstrates that SPR and QCM-D are  
449 suitable techniques for detecting functionalities at the nanocrystal reducing ends, and the  $\Delta D_n$  vs  
450  $\Delta f_n/n$  plots allow to discern the arrangement of nanocrystals at the gold surface. Concluding,  
451 cellulose nanocrystals can be viewed as a good strategy for the step-by-step synthesis of  
452 polymers, especially dendrimers since they act as a solid support that facilitates dendrimer  
453 purification. Indeed, the presence of dendritic structures at the reducing ends dictates their  
454 interaction with gold surfaces, and increase the versatility of cellulose materials.

455

#### 456 *Acknowledgements*

457 This work was financially supported by the French National Research Agency (Project  
458 Cellmach, ANR-17-CE07-0010-01). We greatly thank Dr. Hervé Bizot for the preparation of  
459 tunicate nanocrystals. The authors acknowledge the technical support on DSC from Jean-Eudes  
460 Maigret and the BIBS platform of INRAE for the access to infrared spectroscopy (Sylvie  
461 Durand) and microscopy facilities (Bruno Novales and Angelina D’Orlando).

462

#### 463 *Declaration of competing interest*

464 The authors declare no conflicts of interest.

465

#### 466 **References**

467 Ahola, S., Myllytie, P., Osterberg, M., Teerinen, T., & Laine, J. (2008). Effect of polymer  
468 adsorption on cellulose nanofibril water binding capacity and aggregation. *Bioresources*,  
469 3(4), 1315-1328.



470 Benkaddour, A., Journoux-Lapp, C., Jradi, K., Robert, S., & Daneault, C. (2014). Study of the  
471 hydrophobization of TEMPO-oxidized cellulose gel through two routes: amidation and  
472 esterification process. *Journal of Materials Science*, 49, 2832-2843.

473 Charreau, H., Cavallo, E., & Foresti, M. L. (2020). Patents involving nanocellulose: Analysis of  
474 their evolution since 2010. *Carbohydrate Polymers*, 237.

475 Chemin, M., Moreau, C., Cathala, B., & Villares, A. (2020). Adsorption Behavior of Reducing  
476 End-Modified Cellulose Nanocrystals: A Kinetic Study Using Quartz Crystal  
477 Microbalance. *Journal of Renewable Materials*, 8(1), 29-43.

478 Chemin, M., Moreau, C., Cathala, B., & Villares, A. (2020). Asymmetric modification of  
479 cellulose nanocrystals with PAMAM dendrimers for the preparation of pH-responsive  
480 hairy surfaces. *Carbohydrate Polymers*, 249, 116779.

481 Delepierre, G., Heise, K., Malinen, K., Koso, T., Pitkänen, L., Cranston, E. D., . . . King, A. W.  
482 T. (2021). Challenges in Synthesis and Analysis of Asymmetrically Grafted Cellulose  
483 Nanocrystals via Atom Transfer Radical Polymerization. *Biomacromolecules*, 22(6),  
484 2702-2717.

485 Eichhorn, S. J. (2011). Cellulose nanowhiskers: promising materials for advanced applications.  
486 *Soft Matter*, 7(2), 303-315.

487 Golshan, M., Salami-Kalajahi, M., Roghani-Mamaqani, H., & Mohammadi, M. (2017).  
488 Poly(propylene imine) dendrimer-grafted nanocrystalline cellulose: Doxorubicin loading  
489 and release behavior. *Polymer*, 117, 287-294.

490 Guo, Y. Q., Shen, M. W., & Shi, X. Y. Construction of Poly(amidoamine) Dendrimer/Carbon  
491 Dot Nanohybrids for Biomedical Applications. *Macromolecular Bioscience*.

492 Hassan, M. L. (2006). Preparation and thermal stability of new cellulose-based poly(propylene  
493 imine) and poly(amido amine) hyperbranched derivatives. *Journal of Applied Polymer  
494 Science*, 101(3), 2079-2087.

495 Heise, K., Delepierre, G., King, A., Kostianen, M., Zoppe, J., Weder, C., & Kontturi, E. (2020).  
496 Chemical modification of cellulose nanocrystal reducing end-groups. *Angewandte  
497 Chemie International Edition*, 60(1), 66-87.

498 Heise, K., Kontturi, E., Allahverdiyeva, Y., Tammelin, T., Linder, M. B., Nonappa, & Ikkala, O.  
499 (2020). Nanocellulose: Recent Fundamental Advances and Emerging Biological and  
500 Biomimicking Applications. *Advanced Materials*, 33(3), 2004349.

501 Kishani, S., Vilaplana, F., Ruda, M., Hansson, P., & Wagberg, L. (2020). Influence of Solubility  
502 on the Adsorption of Different Xyloglucan Fractions at Cellulose-Water Interfaces.  
503 *Biomacromolecules*, 21(2), 772-782.

504 Kontturi, K. S., Kontturi, E., & Laine, J. (2013). Specific water uptake of thin films from  
505 nanofibrillar cellulose. *Journal of Materials Chemistry A*, 1, 13655-13663.

506 Lin, F., Cousin, F., Putaux, J.-L., & Jean, B. (2019). Temperature-Controlled Star-Shaped  
507 Cellulose Nanocrystal Assemblies Resulting from Asymmetric Polymer Grafting. *ACS  
508 Macro Letters*, 8, 345-351.

509 Lin, N., & Dufresne, A. (2014). Surface chemistry, morphological analysis and properties of  
510 cellulose nanocrystals with gradiented sulfation degrees. *Nanoscale*, 6(10), 5384-5393.

511 Lin, N., Huang, J., Chang, P. R., Anderson, D. P., & Yu, J. (2011). Preparation, Modification,  
512 and Application of Starch Nanocrystals in Nanomaterials: A Review. *Journal of  
513 Nanomaterials*.

514 Lokanathan, A. R., Lundahl, M., Rojas, O. J., & Laine, J. (2014). Asymmetric cellulose  
515 nanocrystals: thiolation of reducing end groups via NHS-EDC coupling. *Cellulose*, 21(6),  
516 4209-4218.

517 Lokanathan, A. R., Nykanen, A., Seitsonen, J., Johansson, L.-S., Campbell, J., Rojas, O. J., . . .  
518 Laine, J. (2013). Cilia-Mimetic Hairy Surfaces Based on End-Immobilized Nanocellulose  
519 Colloidal Rods. *Biomacromolecules*, 14(8), 2807-2813.

520 Moreau, C., Beury, N., Delorme, N., & Cathala, B. (2012). Tuning the architecture of cellulose  
521 nanocrystal-poly(allylamine hydrochloride) multilayered thin films: Influence of dipping  
522 parameters. *Langmuir*, 28(28), 10425-10436.

523 Nikzamir, M., Hanifehpour, Y., Akbarzadeh, A., & Panahi, Y. Applications of Dendrimers in  
524 Nanomedicine and Drug Delivery: A Review. *Journal of Inorganic and Organometallic*  
525 *Polymers and Materials*.

526 Potthast, A., Radosta, S., Saake, B., Lebioda, S., Heinze, T., Henniges, U., . . . Wetzel, H.  
527 (2015). Comparison testing of methods for gel permeation chromatography of cellulose:  
528 coming closer to a standard protocol. *Cellulose*, 22(3), 1591-1613.

529 Risteen, B., Delepierre, G., Srinivasarao, M., Weder, C., Russo, P., Reichmanis, E., & Zoppe, J.  
530 (2018). Thermally Switchable Liquid Crystals Based on Cellulose Nanocrystals with  
531 Patchy Polymer Grafts. *Small*, 14(46).

532 Rodahl, M., Hook, F., Fredriksson, C., Keller, C. A., Krozer, A., Brzezinski, P., . . . Kasemo, B.  
533 (1997). Simultaneous frequency and dissipation factor QCM measurements of  
534 biomolecular adsorption and cell adhesion. *Faraday Discussions*, 107, 229-246.

535 Sacui, I. A., Nieuwendaal, R. C., Burnett, D. J., Stranick, S. J., Jorfi, M., Weder, C., . . . Gilman,  
536 J. W. (2014). Comparison of the Properties of Cellulose Nanocrystals and Cellulose  
537 Nanofibrils Isolated from Bacteria, Tunicate, and Wood Processed Using Acid,  
538 Enzymatic, Mechanical, and Oxidative Methods. *Acs Applied Materials & Interfaces*,  
539 6(9), 6127-6138.

540 Sauerbrey, G. (1959). Verwendung von Schwingquarzen zur Wägung dünner Schichten und zur  
541 Mikrowägung. *Zeitschrift für Physik*, 155(2), 206-222.

542 Schoch, R. L., & Lim, R. Y. H. (2013). Non-Interacting Molecules as Innate Structural Probes in  
543 Surface Plasmon Resonance. *Langmuir*, 29(12), 4068-4076.

544 Schwanninger, M., Rodrigues, J. C., Pereira, H., & Hinterstoisser, B. (2004). Effects of short-  
545 time vibratory ball milling on the shape of FT-IR spectra of wood and cellulose.  
546 *Vibrational Spectroscopy*, 36(1), 23-40.

547 Shea, F., & Watts, C. E. (1939). Dumas method for organic nitrogen. *Industrial and Engineering*  
548 *Chemistry Analytical Edition*, 11(6), 333-334.

549 Sipahi-Saglam, E., Gelbrich, M., & Gruber, E. (2003). Topochemically modified cellulose.  
550 *Cellulose*, 10(3), 237-250.

551 Tang, C. X., Spinney, S., Shi, Z. Q., Tang, J. T., Peng, B. L., Luo, J. H., & Tam, K. C. (2018).  
552 Amphiphilic Cellulose Nanocrystals for Enhanced Pickering Emulsion Stabilization.  
553 *Langmuir*, 34(43), 12897-12905.

554 Tao, H., Dufresne, A., & Lin, N. (2019). Double-Network Formation and Mechanical  
555 Enhancement of Reducing End-Modified Cellulose Nanocrystals to the Thermoplastic  
556 Elastomer Based on Click Reaction and Bulk Cross-Linking. *Macromolecules*, 52(15),  
557 5894-5906.

- 558 Tao, H., Lavoine, N., Jiang, F., Tang, J., & Lin, N. (2020). Reducing end modification on  
559 cellulose nanocrystals: strategy, characterization, applications and challenges. *Nanoscale*  
560 *Horizons*, 5(4), 607-627.
- 561 Tavakolian, M., Lerner, J., Tovar, F. M., Frances, J., van de Ven, T. G. M., & Kakkar, A. (2019).  
562 Dendrimer directed assembly of dicarboxylated hairy nanocellulose. *Journal of Colloid*  
563 *and Interface Science*, 541, 444-453.
- 564 Tehrani, A. D., & Basiryan, A. (2015). Dendronization of cellulose nanowhisker with cationic  
565 hyperbranched dendritic polyamidoamine. *Carbohydrate Polymers*, 120, 46-52.
- 566 Terech, P., Chazeau, L., & Cavaille, J. Y. (1999). A small-angle scattering study of cellulose  
567 whiskers in aqueous suspensions. *Macromolecules*, 32(6), 1872-1875.
- 568 Villares, A., Moreau, C., & Cathala, B. (2018). Star-like Supramolecular Complexes of  
569 Reducing-End-Functionalized Cellulose Nanocrystals. *Acs Omega*, 3(11), 16203-16211.
- 570 Wang, N., Ding, E. Y., & Cheng, R. S. (2007). Thermal degradation behaviors of spherical  
571 cellulose nanocrystals with sulfate groups. *Polymer*, 48(12), 3486-3493.
- 572 Wang, Y. C., & Lu, Q. Y. (2020). Dendrimer functionalized nanocrystalline cellulose for Cu(II)  
573 removal. *Cellulose*, 27(4), 2173-2187.
- 574 Zhao, Y., & Li, J. (2014). Excellent chemical and material cellulose from tunicates: diversity in  
575 cellulose production yield and chemical and morphological structures from different  
576 tunicate species. *Cellulose*, 21(5), 3427-3441.
- 577 Zhao, Y. D., Zhang, Y. J., Lindstrom, M. E., & Li, J. B. (2015). Tunicate cellulose nanocrystals:  
578 Preparation, neat films and nanocomposite films with glucomannans. *Carbohydrate*  
579 *Polymers*, 117, 286-296.
- 580 Zoppe, J. O., Dupire, A. V. M., Lachat, T. G. G., Lemal, P., Rodriguez-Lorenzo, L., Petri-Fink,  
581 A., . . . Klok, H.-A. (2017). Cellulose Nanocrystals with Tethered Polymer Chains:  
582 Chemically Patchy versus Uniform Decoration. *Acs Macro Letters*, 6(9), 892-897.

583